International Journal of Heat and Mass Transfer 150 (2020) 119345

Contents lists available at ScienceDirect

International Journal of Heat and Mass Transfer

journal homepage: www.elsevier.com/locate/hmt

A curved lattice Boltzmann boundary scheme for thermal convective flows with Neumann boundary condition

Shi Tao[a,*], Ao Xu[b], Qing He[a], Baiman Chen[a,*], Frank G.F. Qin[a]

[a] Key Laboratory of Distributed Energy Systems of Guangdong Province, Dongguan University of Technology, Dongguan 523808, China
[b] National Key Laboratory of Science and Technology on Aerodynamic Design and Research, School of Aeronautics, Northwestern Polytechnical University, Xi'an 710072, China

ARTICLE INFO

Article history:
Received 26 June 2019
Revised 8 January 2020
Accepted 8 January 2020

Keywords:
Lattice Boltzmann method
Thermal flows
Curved boundary condition
Heat flux at interface
Second-order accuracy

ABSTRACT

We propose a curved lattice Boltzmann boundary scheme for thermal convective flows with Neumann boundary condition. The distribution function at the fluid-solid intersection node is obtained to accomplish the interpolation of unknown temperature distribution function at the boundary point. Specifically, the distribution function is first extrapolated from the fluid point along the lattice link; and then, the one in the opposite direction is evaluated by the anti-bounce back rule with wall temperature, which can be further determined by the specified Neumann boundary condition at the fluid-solid interface. The advantage of our scheme is that the involved inter/extrapolations are completely link-based, resulting in a quite efficient implementation procedure. Furthermore, our scheme has second-order spatial accuracy, and we verified in four numerical examples where analytical solutions are available: the heat transfer in a channel with a sinusoidal temperature gradient, the thermal diffusion in an annulus, and the conjugate heat transfer for these two cases. To further validate our scheme for thermal convective flow problems with complex geometries, we simulate the natural convection in an annulus, the thermal flow past a cylinder, and the mixed convection in a lid-driven cavity with a circular enclosure. The simulation results are consistent with existing benchmark data obtained by other methods.

1. Introduction

In the past three decades, the lattice Boltzmann method (LBM) has been developed as a convenient solver for the Navier-Stokes (N-S) equations to simulate fluid flow problems [1,2]. To describe fluid flows coupled with heat transfer, the convection-diffusion (CD) equation is further combined with the N-S equations. Due to the advantages of the LB method including easy implementation and parallelization [3], efforts have been devoted to extending the LB method to thermal convective flow problems [4,5], for example, the double distribution function approach which consists of the velocity distribution function and temperature distribution function to solve the CD equation. The double distribution function approach has excellent numerical stability, and it has been used for natural, forced and mix convection flows [6,7].

Different types of boundary condition between fluid and solid interface should be handled when simulating thermal convective flows, which is transformed to identify the unknown distribution function coming from the solid zone during the streaming step in LBM. For straight and curved surfaces, a lot of hydrodynamic boundary schemes have been proposed when using the LBM to solve the N-S equations. The no-slip velocity boundary condition in that scenario can be easily enforced through the simple bounce-back (BB) scheme [8], the interpolated bounce-back scheme [9], and the non-equilibrium extrapolation (NEE) scheme [10]. It should be noted that the latter two schemes are specially designed for curved boundaries, where a relative distance from the boundary to the interface is introduced to improve the spatial accuracy compared with that of simple BB scheme. In the case of thermal convective flows, the CD equation should be solved with specified temperature or heat flux boundary condition (i.e., the Dirichlet or Neumann boundary condition) between the fluid-solid interface.

If the wall temperature is known (i.e., the Dirichlet boundary condition), the treatment for straight and curved boundaries are similar to the hydrodynamic counterpart. For instance, the NEE scheme proposed by Guo et al. [10] has been applied to simulate the unsteady Taylor-Couette flow [11], the heat transfer in a cavity [12], and the natural convection in eccentric annulus [13], respectively. Khazaeli et al. [14] and Mohsen et al. [15] also presented the thermal version of the hydrodynamic ghost fluid (GF) scheme proposed by Tiwari et al. [16]. It should be noted that both the exten-

* Corresponding authors.
E-mail addresses: taoshi@dgut.edu.cn (S. Tao), chenbm@dgut.edu.cn (B. Chen).

https://doi.org/10.1016/j.ijheatmasstransfer.2020.119345
0017-9310/

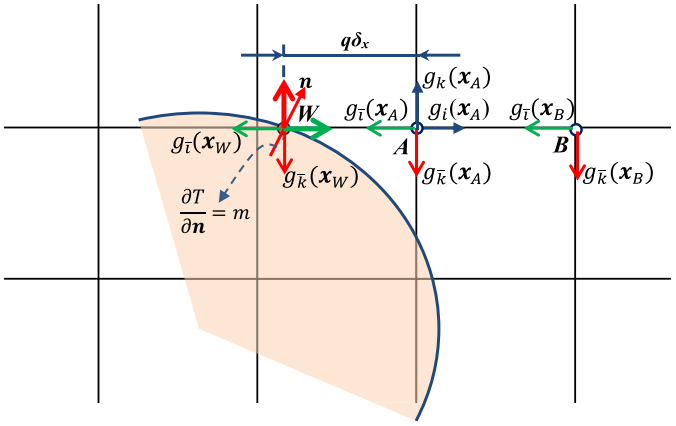

Fig. 1. Schematic of the current curved Neumann boundary condition. $\boldsymbol{x}_A$ is the boundary node with unknown distribution functions. $\boldsymbol{x}_W$ and $\boldsymbol{x}_B$ are the intersection point and the nearest fluid node along the intersection direction, respectively.

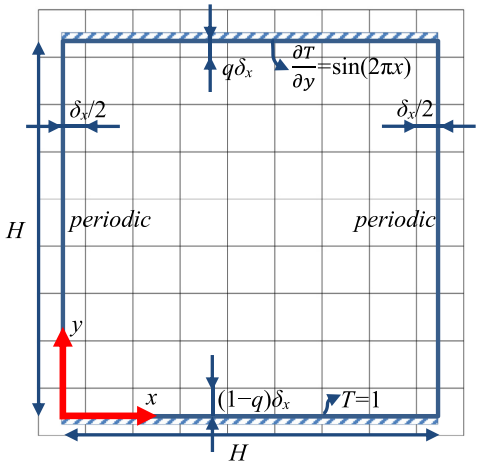

Fig. 2. Schematic of the channel and the boundary conditions.

sions mentioned above decompose the distribution function into the equilibrium and the non-equilibrium parts. The former portion is obtained by the interpolated macroscopic quantities, while the latter portion is evaluated through extrapolation. Therefore, both NEE and GF schemes fall into the non-equilibrium extrapolation-type schemes, and their extensions to the thermal convective flows are quite straightforward. However, significant modifications are needed to develop thermal boundary conditions based on the simple BB schemes. Zhang et al. [17] first demonstrated that the anti-bounce back rule should replace the original one in thermal convective flows. However, in their boundary scheme, the relative distance from the boundary to the interface was not involved, and it was essentially a simple anti-bounce back method with the first-order accuracy for curved geometries. Chen et al. [18] subsequently improved that approach with an interpolated temperature at the middle of a lattice link, and they showed the modified scheme has second-order accuracy for the temperature field.

There are also many thermal convective flow problems where the macroscopic constraint is heat flux at the fluid-solid interface, i.e., the Neumann type boundary condition [38,39]. Due to the simplicity in the Dirichlet boundary treatment, it is straightforward to identify the boundary temperature and then transform the Neumann type into the Dirichlet type boundary conditions. Hence, the normal derivative in the macroscopic heat flux constraint was replaced with various finite difference schemes in previous studies. Liu et al. [19] reported a three-point scheme for the straight thermal wall to obtain the surface temperature. For curved geometries, Zhang et al. [17] proposed a simple anti-bounce back method, in which a first-order finite difference scheme was applied to calculate the heat flux and arbitrarily evaluated along with the lattice link. However, heat flux is temperature derivative in the normal direction, and it generally not consistent with the lattice link. Due to such surface heterogeneity, Chen et al. [18] modified the above simple BB scheme with an interpolated rebounding temperature and normally discretized heat flux with the same first-order finite difference method. A bilinear interpolation scheme computed the unknown fluid temperature. Due to the first-order approximation of normal derivative, those mentioned above finite difference-based schemes [17,18] are just first-order spatial accurate for the Neumann boundary conditions. Note that recently one more interpolation point is introduced to approximate the temperature derivative at the interface [41,42]. On the other hand, the asymptotic analysis technique was used to construct the Neumann schemes. The unknown distribution function was considered to be a combination of several known distribution functions, and their weights were determined through the asymptotic theory. Huang et al. [20] first proposed a one-point Neumann scheme for the curved boundaries; however, their scheme suffers from low accuracy and numerical instability issues. They subsequently presented an improved version with second-order spatial accuracy [21]. In Huang et al.'s scheme, the curved boundary was approximated by zig-zag lines, and the normal derivative at the boundary node was evaluated with the combination of first- and second-order normal derivatives of the auxiliary points. The implementation procedure was complicated and difficult to be applied in the simulation of complex thermal convective flows [22,23]. Li et al. [24,25] proposed a Neumann boundary condition based on the asymptotic theory. They convert the normal direction of the boundary into derivative conditions in the lattice link directions; however, their scheme involves complex analysis of topological geometric and is of first-order spatial accuracy.

The above-mentioned finite difference and asymptotic analysis-based Neumann boundary schemes generally suffer low accuracy and complicated implementation procedure. In this work, we aim to propose an efficient second-order accurate Neumann scheme for thermal convective flows with complex geometries. The macroscopic heat flux constraint is evaluated by the moment of the non-equilibrium distribution functions. With the distribution functions at the fluid-solid interface obtained by second-order extrapolation and anti-bounce back rule, the wall temperature can be determined through the root-finding. The unknown distribution function is then interpolated from the distribution functions along with a lattice link. The remaining part of the paper is organized as follows: In Section 2, we provide the numerical method; in Section 3, we validate the proposed numerical scheme through seven examples; in Section 4, we summarize the main conclusions of the present work.

2. Numerical method

The incompressible viscous thermal flow is generally subjected to the N-S and CD equations as

$$\nabla.\boldsymbol{u} = 0, \tag{1}$$

$$\frac{\partial \boldsymbol{u}}{\partial t} + \boldsymbol{u}.\nabla\boldsymbol{u} = -\frac{1}{\rho}\nabla p + \nu\nabla^2\boldsymbol{u} + \boldsymbol{a}_g, \tag{2}$$

$$\frac{\partial T}{\partial t} + \nabla.(\boldsymbol{u}T) = \kappa\nabla^2 T, \tag{3}$$

where $\boldsymbol{u}$, ρ, p, ν, T and κ are the velocity, density, pressure, kinetic viscosity, temperature and thermal diffusivity of fluid, respectively.

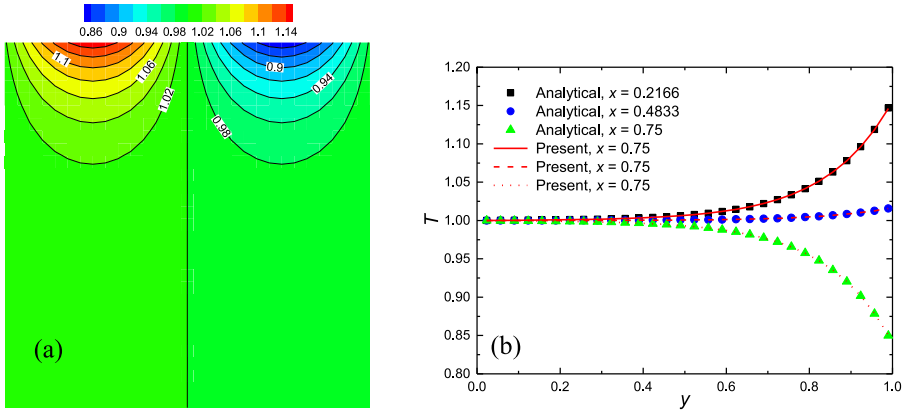

Fig. 3. Isotherms (a) and the temperature profiles at three positions (b) for the channel with $\tau_T = 0.6$, $q = 0.2$ and $N = 30$.

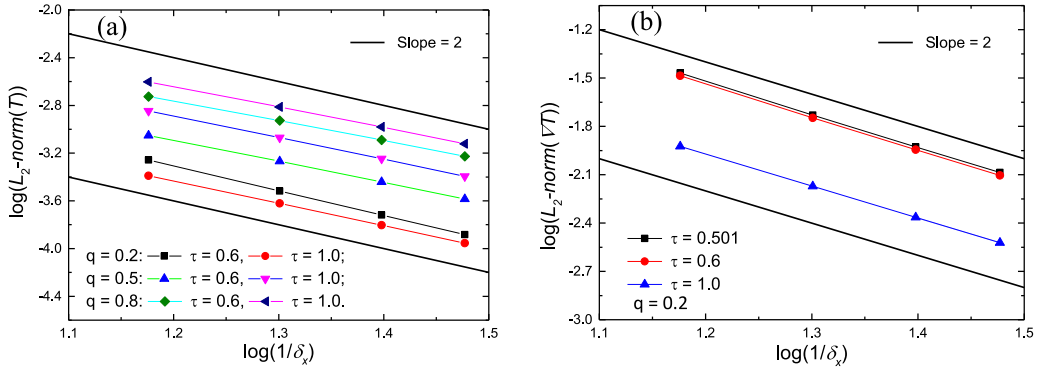

Fig. 4. The convergence rates of the temperature (a) and the temperature gradient (b) with different grid resolutions.

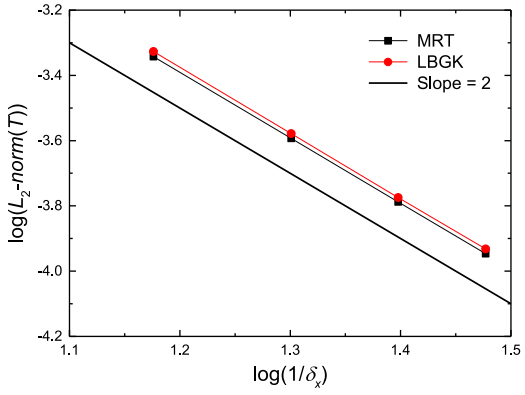

Fig. 5. The convergence rates with the LBGK and MRT collision models at $\tau_T = 0.6$ and $q = 0.3$.

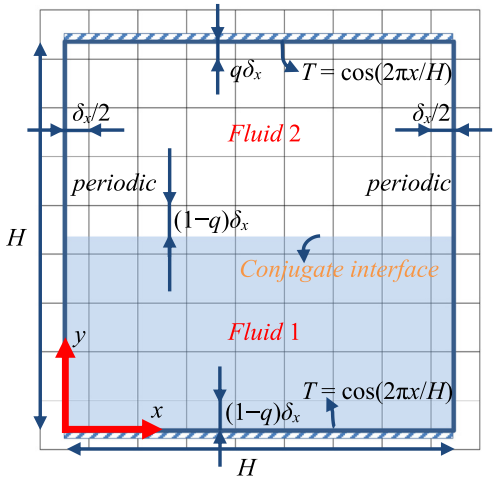

Fig. 6. Schematic of two-fluid channel with convection-diffusion process.

In the momentum equation, the body force $\boldsymbol{a}_g$ is for introducing the buoyancy force from the temperature filed. With the Boussinesq approximation, it is usually expressed as

$$\boldsymbol{a}_g = g_0\alpha(T - T_0)\boldsymbol{j}. \tag{4}$$

Here, g_0 is the acceleration of gravity, α is the thermal expansion coefficient, T_0 is the average temperature of the fluid, and $\boldsymbol{j}$ is the unit vector in the vertical direction.

2.1. Lattice Boltzmann method for fluid flows and heat transfer

The double distribution population approach is considered to be capable of a wide range of temperature variations and has excellent numerical stability [7,26,27]. It is hence implemented in the present study to solve the above N-S and CD equations, where two sets of distribution functions, $f_i(\boldsymbol{x}, t)$ and $g_i(\boldsymbol{x}, t)$ for the velocity and temperature fields are adopted, respectively

$$f_i(\boldsymbol{x} + \boldsymbol{e}_i\delta_t,\ t + \delta_t) - f_i(\boldsymbol{x},\ t) = -\left(\boldsymbol{M}^{-1}\boldsymbol{S}\boldsymbol{M}\right)_{ij}\left(f_j - f_j^{eq}\right) + \delta_t\boldsymbol{F}_i,$$
$$\times i = 0,\ 1,\ \ldots, 8. \tag{5}$$

$$g_i(\boldsymbol{x} + \boldsymbol{e}_i\delta_t,\ t + \delta_t) - g_i(\boldsymbol{x},\ t) = -\frac{1}{\tau_T}\left(g_j - g_j^{eq}\right), \quad i = 0,\ 1,\ \ldots, 4. \tag{6}$$

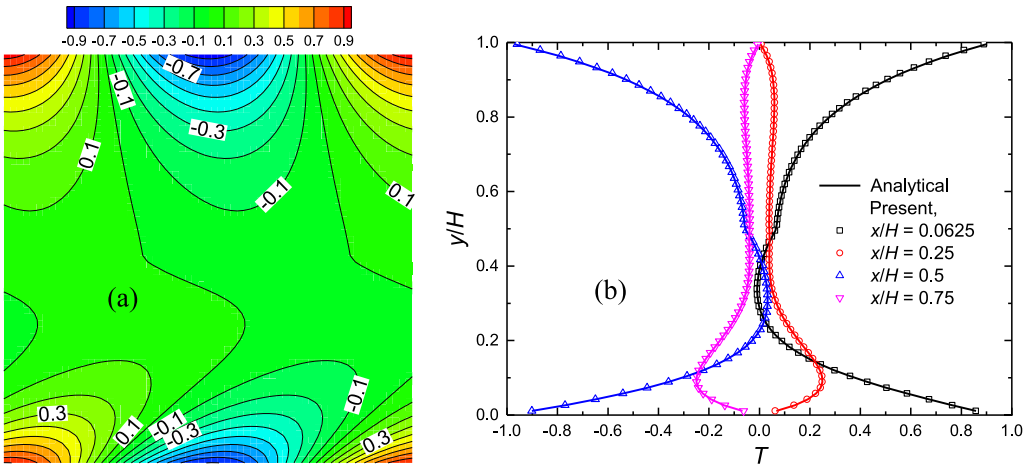

Fig. 7. Isotherms (a) and the temperature profiles at three positions (b) for the channel flow with $q = 0.3$.

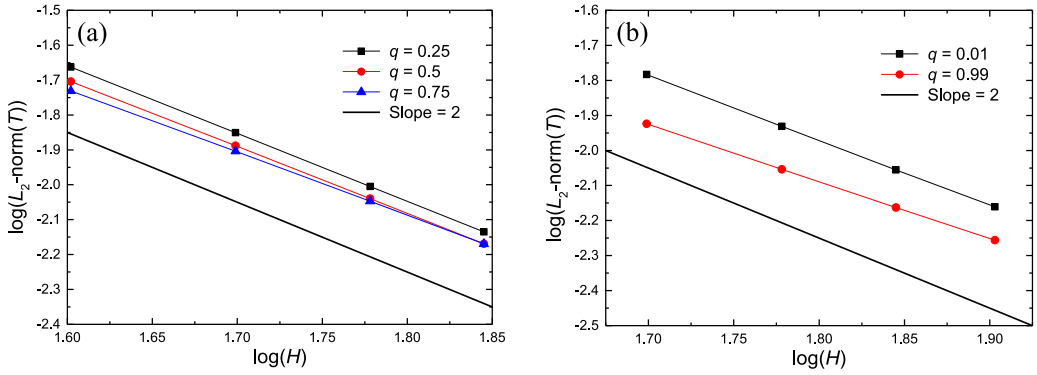

Fig. 8. The convergence rates of the temperature at $q = (0.25, 0.5, 0.75)$ (a) and $q = (0.01, 0.99)$ (b) with different grid resolutions. $H = 1/\delta_x$.

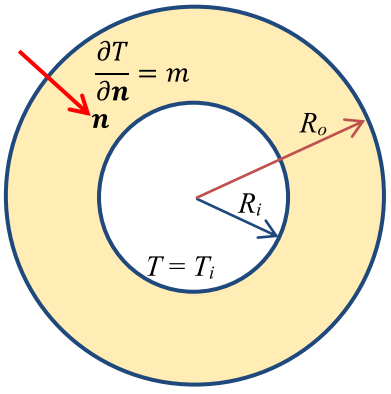

Fig. 9. Schematic of the pure diffusion between two concentrated cylinders.

Here, $\boldsymbol{e}_i$ is the lattice velocity, $\boldsymbol{x}$ the position, t the time, and δ_t is the temporal step. $\boldsymbol{M}$ is the transform matrix and $\boldsymbol{S}$ the relaxation matrix in the multi-relaxation-time (MRT) collision model [28]. f^{eq} and g^{eq} are the Maxwellian-type equilibrium distribution functions, which are typically evaluated by the density ρ, velocity $\boldsymbol{u}$ and temperature T of the fluid as

$$f_j^{eq} = \omega_j \rho \left[1 + \frac{\boldsymbol{e}_j.\boldsymbol{u}}{c_s^2} + \frac{(\boldsymbol{e}_j.\boldsymbol{u})^2}{2c_s^4} - \frac{\boldsymbol{u}^2}{2c_s^2}\right], \quad g_j^{eq} = \omega_j T\left[1 + \frac{\boldsymbol{e}_j.\boldsymbol{u}}{c_s^2}\right], \tag{7}$$

where ω_j is the weight coefficient; $c_s = \sqrt{RT}$ is the lattice sound speed and set to be $1/\sqrt{3}$ (R is the gas constant, and $\delta_x/\delta_t = 1$ in this paper with δ_x the lattice spacing). For consistency, the force term of $\boldsymbol{F}_i$ for incorporating the buoyancy force $\boldsymbol{a}_g$ should be given by [29]

$$\boldsymbol{F} = \boldsymbol{M}^{-1}(\boldsymbol{I} - \boldsymbol{S}/2)\boldsymbol{M}\bar{\boldsymbol{F}}, \tag{8}$$

where $\boldsymbol{I}$ is the identity matrix, $\boldsymbol{F} = (F_0, F_1, \ldots, F_8)$, and $\bar{\boldsymbol{F}} = (\bar{F}_0, \bar{F}_1, \ldots, \bar{F}_8)$ with

$$\bar{F}_i = w_i\left[\frac{\boldsymbol{e}_i.\boldsymbol{a}_g}{c_s^2} + \frac{\boldsymbol{u}\boldsymbol{a}_g : (\boldsymbol{e}_i\boldsymbol{e}_i - c_s^2\boldsymbol{I})}{c_s^4}\right], \quad i = 0, 1, \ldots, 8. \tag{9}$$

For simplicity and without loss of generality, the D2Q9 and D2Q5 velocity models [24,37] are employed respectively for the velocity and temperature fields. Through Chapman-Enskog expansion, the macroscopic quantities, i.e., ρ, $\boldsymbol{u}$, p, ν, T and κ can be respectively obtained as

$$\rho = \sum_{i=0}^{8} f_i, \ \rho\boldsymbol{u} = \sum_{i=0}^{8} \boldsymbol{e}_i f_i + \delta_t \boldsymbol{a}_g/2, \ p = \rho c_s^2, \ \nu = c_s^2(\tau_s - 0.5)\delta_t,$$
$$\times T = \sum_{i=0}^{8} g_i, \ \kappa = c_s^2(\tau_T - 0.5)\delta_t. \tag{10}$$

Note that the LBGK collision model in Eq. (6) is used for solving the CD equation in the present study. It can be replaced with a corresponding MRT model and is rewritten as [43]

$$g_i(\boldsymbol{x} + \boldsymbol{e}_i\delta_t, \ t + \delta_t) - g_i(\boldsymbol{x}, \ t) = -\left(\boldsymbol{N}^{-1}\boldsymbol{\Lambda}\boldsymbol{N}\right)_{ij}\left(g_j - g_j^{eq}\right)_i, \quad i = 0, \ 1, \ \ldots, 4. \tag{11}$$

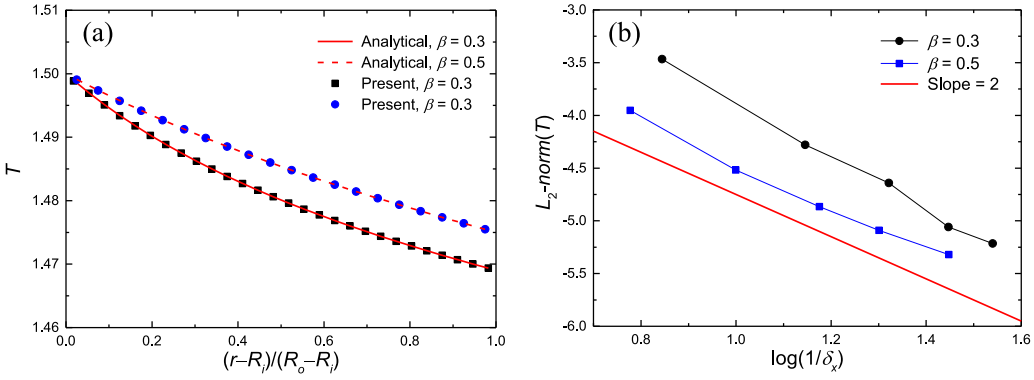

Fig. 10. The temperature profile between the cylinders (a) and the convergence rate (b) at two radius ratios.

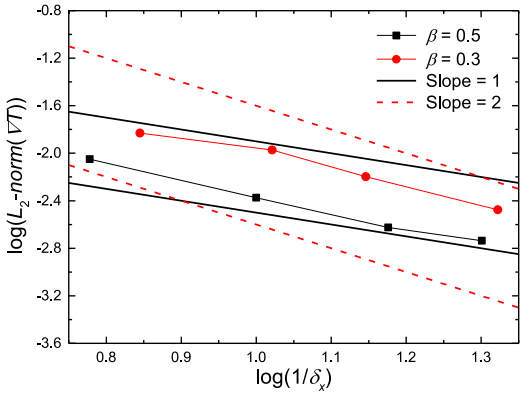

Fig. 11. The convergence rate of the temperature gradient with different grid resolutions at $\beta = 0.3$ and 0.5.

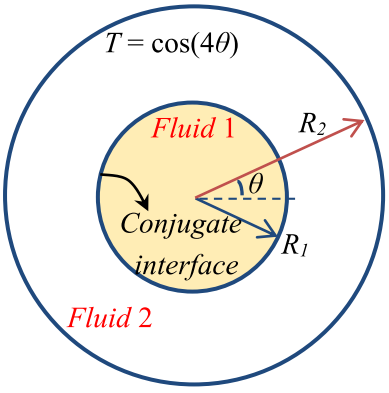

Fig. 12. Schematic of the heat transfer in two concentrated cylinders with a conjugate interface.

where $\boldsymbol{N}$ and $\boldsymbol{\Lambda}$ are respectively the transform and relaxation matrixes as

$$\boldsymbol{N} = \begin{bmatrix} 1 & 1 & 1 & 1 & 1 \\ 0 & 1 & 0 & -1 & 0 \\ 0 & 0 & 1 & 0 & -1 \\ 0 & 1 & -1 & 1 & -1 \\ -4 & 1 & 1 & 1 & 1 \end{bmatrix}, \quad \boldsymbol{\Lambda} = diag(1,\ 1/\tau_T, 1/\tau_T, 1/\tau_3,\ 1/\tau_3). \tag{12}$$

2.2. Neumann boundary condition at the curved boundary

The treatment of Neumann boundary condition at the curved fluid-solid interface is frequently encountered in the complex thermal convective flows using LBM. Similar to the Dirichlet counterpart, the main concern is to identify the unknown distribution function (UDF) at the boundary node, which has at least one lattice link with the nodes at the opposite side of the interface.

Distribution functions in several directions at the boundary node are unknown after the streaming step in LBM. Taking point A depicted in Fig. 1 as an example, the g_1 and g_2 are UDFs. To obtain $g_i(\boldsymbol{x}_A)$, the lattice link interpolation scheme can be applied as

$$g_i(\boldsymbol{x}_A) = \frac{1}{1+q}(g_i(\boldsymbol{x}_W) + qg_i(\boldsymbol{x}_B)), \tag{13}$$

where $g_i(\boldsymbol{x}_B)$ is known and $g_i(\boldsymbol{x}_W)$ is unknown. The unknown $g_i(\boldsymbol{x}_W)$ can be obtained by the anti-bounce back scheme as [17,18,31]

$$g_i(\boldsymbol{x}_W) = -g_{\bar{i}}(\boldsymbol{x}_W) + 2\omega_i T(\boldsymbol{x}_W), \tag{14}$$

where $T(\boldsymbol{x}_w)$ is the wall temperature at the intersection point W. However, two more unknowns, i.e., $g_{\bar{i}}(\boldsymbol{x}_W)$ and $T(\boldsymbol{x}_w)$ are further introduced. In this study, a second-order extrapolation scheme is used to obtain the first variable,

$$g_{\bar{i}}(\boldsymbol{x}_W) = (1+q)g_{\bar{i}}(\boldsymbol{x}_A) - qg_{\bar{i}}(\boldsymbol{x}_B). \tag{15}$$

Note that the streaming procedure can directly obtain $g_{\bar{i}}(\boldsymbol{x}_A)$ and $g_{\bar{i}}(\boldsymbol{x}_B)$. Similarly, we have

$$g_k(\boldsymbol{x}_W) = -g_{\bar{k}}(\boldsymbol{x}_W) + 2\omega_k T(\boldsymbol{x}_W), \tag{16}$$

$$g_{\bar{k}}(\boldsymbol{x}_W) = (1+q)g_{\bar{k}}(\boldsymbol{x}_A) - qg_{\bar{k}}(\boldsymbol{x}_B). \tag{17}$$

Furthermore, the distribution function at $\boldsymbol{e}_0 = (0, 0)$ is

$$g_0(\boldsymbol{x}_W) = \omega_0 T(\boldsymbol{x}_W). \tag{18}$$

So far, we can find from Eqs. (14)–(18) that at the intersection point W, the distribution functions are just determined by the temperature $T(\boldsymbol{x}_W)$.

On the other hand, for the Neumann boundary condition, the macroscopic constraint is the normal derivative of temperature at the fluid-solid interface, i.e.,

$$\frac{\partial T(\boldsymbol{x}_W)}{\partial \boldsymbol{n}} = m, \tag{19}$$

where $\boldsymbol{n} = (n_x,\ n_y)$ is a unit vector normal to the interface and pointing to the fluid zone, and m is a known parameter. Eq. (19) can be rewritten as

$$\boldsymbol{n} \cdot \nabla T(\boldsymbol{x}_W) = m. \tag{20}$$

The temperature gradient is evaluated by the moment of the non-equilibrium distribution functions with a second-order accuracy as [22,23,23,45]

$$\nabla T = -\frac{1}{c_s^2 \tau_T \delta_t} \sum_i \boldsymbol{e}_i [g_i - g^{eq}] = \frac{-1}{c_s^2 \tau_T \delta_t} \left(\sum_{l=0}^{4} \boldsymbol{e}_l g_l - \boldsymbol{u} \sum_{l=0}^{4} g_l \right). \tag{21}$$

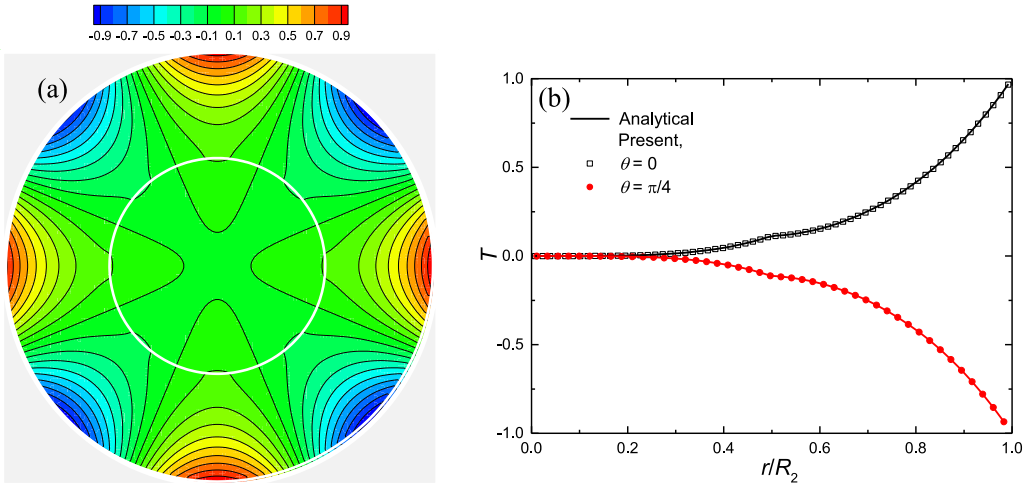

Fig. 13. Isotherms (a) and the temperature profile between the cylinders at $\theta = 0$ and $\pi/4$ (b) with $\beta = 0.5$.

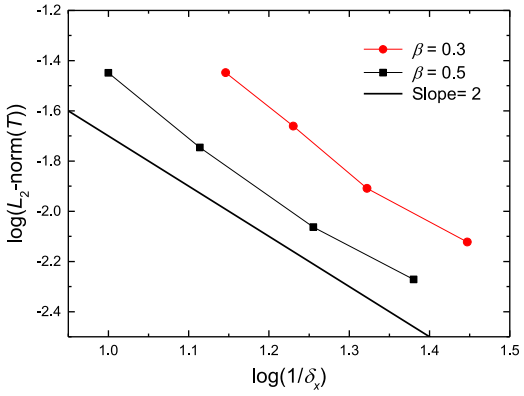

Fig. 14. The convergence rate of the temperature with different grid resolutions at $\beta = 0.3$ and 0.5.

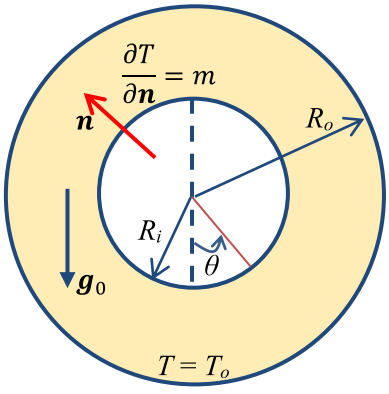

Fig. 15. Schematic of the natural convection between two concentrated cylinders.

Then, we have

$$(n_x,\ n_y)\cdot\left(e_{i,0}g_i(\boldsymbol{x}_W)+e_{\bar{i},0}g_{\bar{i}}(\boldsymbol{x}_W)-u_xT(\boldsymbol{x}_W),\ e_{k,1}g_k(\boldsymbol{x}_W)\right.$$
$$\left.+e_{\bar{k},1}g_{\bar{k}}(\boldsymbol{x}_W)-u_yT(\boldsymbol{x}_W)\right)=-c_s^2\tau_T\delta_t m, \tag{22}$$

with $\boldsymbol{e}_i = (e_{i,0},\ e_{i,1})$. Substituting the Eqs. (14)–(18) into Eq. (22), the interface temperature can be finally determined as

$$T(\boldsymbol{x}_W)=\frac{c_s^2\tau_T\delta_t m+2e_{i,0}g_{\bar{i}}(\boldsymbol{x}_W)n_x+2e_{k,1}g_{\bar{k}}(\boldsymbol{x}_W)n_y}{(2\omega_i e_{i,0}-u_x)n_x+\left(2\omega_k e_{k,1}-u_y\right)n_y}. \tag{23}$$

Once the wall temperature is obtained, $g_i(\boldsymbol{x}_W)$ is computed by Eq. (14). With $g_i(\boldsymbol{x}_W)$ at hand, the UDF, i.e., $g_i(\boldsymbol{x}_A)$ can be finally interpolated from Eq. (13).

The linear inter/extrapolations, as can be seen in Eqs. (13), (15) and (17) achieve second-order accuracy. The anti-bounce back scheme in Eqs. (14) and (16) is also second-order accurate. Furthermore, the computation of the temperature gradient by Eq. (21) through the moment of the non-equilibrium distribution functions has second-order accuracy. Therefore, the present Neumann scheme is theoretically of second-order spatial accuracy. Another advantage of this scheme is that the involved inter/extrapolations are all based on the directions of the lattice link, which contributes to the easy implementation in the thermal convective flow simulations. Note that the present scheme is independent of the collision models in LBM, because of the two essential ingredients of it, i.e., the anti-bounce back rule in Eq. (14) and the distribution-function-based temperature gradient in Eq. (21) can be applied consistently to the LBGK and MRT models. Furthermore, with the inter/extrapolations implemented to both sides of the conjugate interface (see Figs. 6 and 8), the interface temperature T_W can be determined, and hence the conjugate boundary condition (Eq. (26)) can also be handled by the present scheme.

3. Results and discussion

In this section, we validate the current Neumann scheme through seven numerical tests. We first simulate the heat transfer in a channel with a sinusoidal temperature gradient, and the thermal diffusion between circular surfaces to test the spatial accuracy of the scheme, where analytical results are available. We then simulate thermal convective flows with complex geometries, including the natural convection in an annulus, the thermal flow past a cylinder, and the mix-convection in a lid-driven cavity with a circular closure. In these tests, the single-node no-slip velocity boundary scheme [32] is adopted for the N-S equations; the single-node Dirichlet temperature boundary scheme proposed in our previous work [40] is chosen for the CD equation with specified temperature boundary. The LBGK model is used in the simulations unless otherwise specified.

3.1. Heat transfer in a channel with a sinusoidal temperature gradient

As illustrated in Fig. 2, the height and length of the channel are both $H = 1$, which is resolved by N lattices in the simulations. A

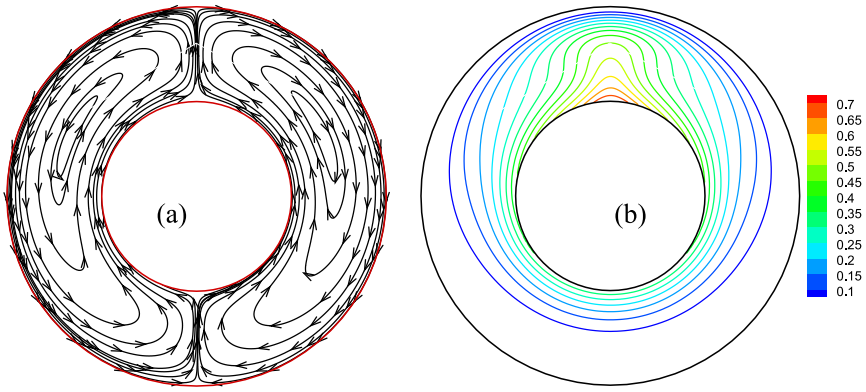

Fig. 16. Isotherms (a) and streamlines (b) of the natural convection in an annulus with an inner Neumann surface, at $Pr = 0.7$ and $Ra = 5700$.

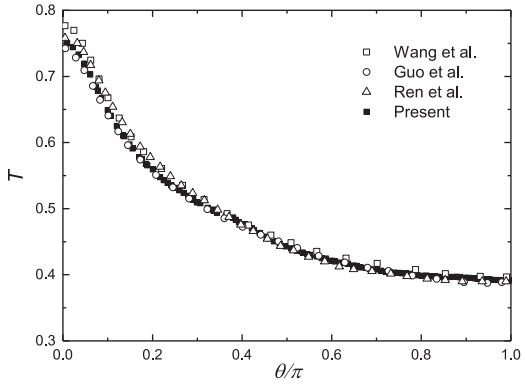

Fig. 17. The distribution of the temperature along the surface of the inner cylinder.

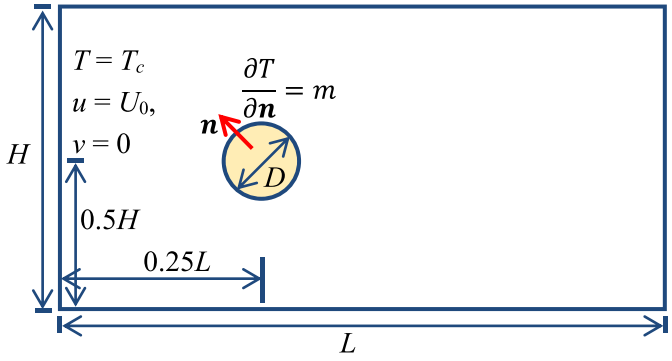

Fig. 18. Schematic of the thermal flow around a cylinder with a fixed heat flux at the surface.

temperature gradient in the sine form $\partial T/\partial y = \sin(2\pi x)$ is imposed on the upper wall. With x ranging from 0 to 1, the upper wall experiences a whole period of the gradient. The temperature of the lower wall is constant with $T = 1$, which deviates from the second row of grids with an offset of $(1 - q)\delta_x$. The left and right sides of the channel are periodic boundaries, and they locate at the middle of the lattices. The analytical solution of the temperature field is

$$T(x,\ y) = 1 + \frac{\sin(2\pi x)\sinh(2\pi y)}{2\pi\cosh(2\pi)}. \tag{24}$$

Fig. 3 presents the isotherms and temperature profiles in the channel at $\tau_T = 0.6$, $q = 0.2$ and $N = 30$. It can be observed that the results agree well with the analytical solutions. Furthermore, simulations with different grid resolutions are performed to study the convergence rate of the temperature field, which is defined as

$$L_2 - norm(T) = \sqrt{\frac{\sum (T_{LB}(\boldsymbol{x}) - T_a(\boldsymbol{x}))^2}{\sum (T_a(\boldsymbol{x}))^2}}, \tag{25}$$

where T_a is the analytical solution of temperature given by Eq. (24), T_{LB} is obtained by the LBM with the present Neumann scheme, and $\boldsymbol{x}$ is for all the fluid nodes. The error of the temperature gradient is further defined to evaluate the numerical accuracy of the current scheme,

$$L_2 - norm(\nabla T) = \sqrt{\frac{\sum (\nabla T_{LB}(\boldsymbol{x}) - \nabla T_a(\boldsymbol{x}))^2}{\sum (\nabla T_a(\boldsymbol{x}))^2}}, \tag{26}$$

where ∇T_a and ∇T_{LB} are the gradients of temperature calculated by the Eq. (21) locally and Eq. (24) with a second-order finite difference scheme. According to Zhang et al. [23], $\boldsymbol{x}$ in Eq. (26) is for all the internal fluid nodes, namely the boundary node that has a lattice link intersecting with walls is excluded in the Eq. (26). Fig. 4(a) and (b) show the relative errors of the temperature and its gradient. It is clear that the convergence rates are all close to 2, and a second-order spatial accuracy of the present scheme is then generally confirmed.

The effect of the collision model on the accuracy of the present scheme is further tested in this flow problem. The simulations are performed at $\tau_T = 0.6$ and $q = 0.3$. The other relaxation time τ_3 is set to be 1.5 [43]. From the results depicted in Fig. 5, it is observed that both models achieve second-order spatial accuracy.

3.2. A two-fluid channel with convection-diffusion processes

We further consider the convection-diffusion process in a channel with two fluids, where the geometry arrangement is the same as that of the one-fluid case mentioned above. The fluids are separated from the conjugate interface at $y = 0.5H$, where the boundary condition is specified as

$$T_1 = T_2 = T_y, \quad \kappa_1 \left.\frac{\partial T}{\partial n}\right|_1 = \sigma\kappa_2 \left.\frac{\partial T}{\partial n}\right|_2, \quad y = 0.5H, \tag{26a}$$

Here, the subscripts 1 and 2 denote the fluid 1 and fluid 2, respectively. $\sigma = 1$ is the volume heat capacity ratio. The boundary conditions at the top and bottom walls are T ($y = 0$ and H) $= \cos(2\pi x/H)$. A constant velocity $\boldsymbol{u} = (U_0, 0)$ is applied to the entire computational domain. The analytical solution for the temperature in the channel is expressed as [44]

$$T(x,y) = \begin{cases} \mathrm{Re}\left\{e^{ikx}\left[\gamma_1 e^{-\lambda_1 y} + (1-\gamma_1)e^{\lambda_1 y}\right]\right\}, & 0 \le y \le 0.5H, \\ \mathrm{Re}\left\{e^{ikx}\left[\gamma_2 e^{-\lambda_2 y} + (1-\gamma_2 e^{-\lambda_2 H})e^{-\lambda_2(H-y)}\right]\right\}, & 0.5H \le y \le H, \end{cases} \tag{27}$$

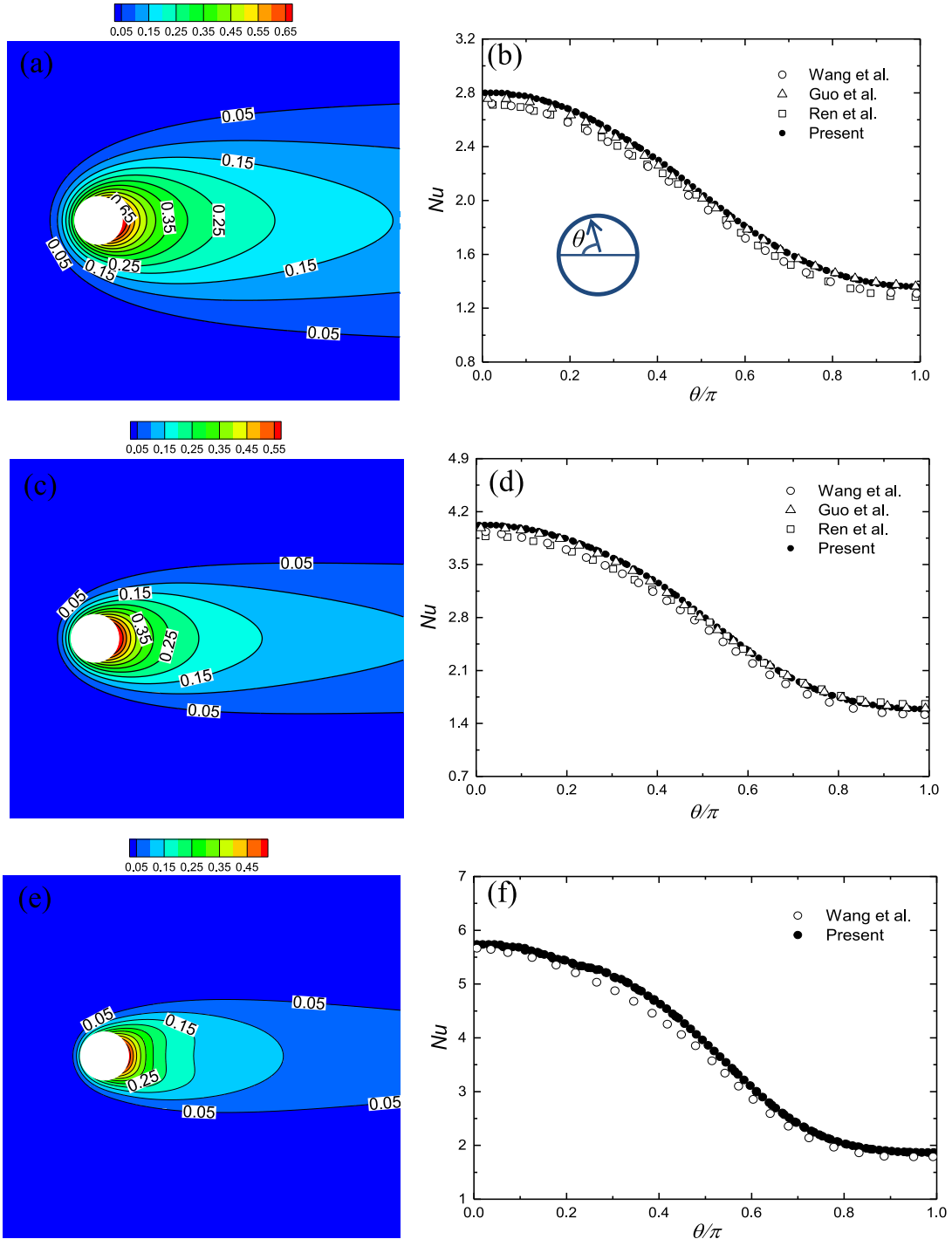

Fig. 19. Isotherms around the cylinder (left column) and the distribution of *Nu* along the cylinder surface (right column). The $Re = 10$ (a, b), $Re = 20$ (c, d) and $Re = 40$ (e, f).

where

$$\gamma_1 = \frac{\lambda_1(a_3^2 - a_2^2) + \chi\sigma\lambda_2(2a_1a_2a_3 - a_2^2 - a_3^2)}{(\lambda_1 + \chi\sigma\lambda_2)(a_1^2a_3^2 - a_2^2) - (\lambda_1 - \chi\sigma\lambda_2)(a_1^2a_2^2 - a_3^2)},$$

$$\gamma_2 = \frac{\lambda_1(a_1^2a_3 + a_3 - 2a_1a_2) + \chi\sigma\lambda_2(a_1^2 - 1)}{(\lambda_1 + \chi\sigma\lambda_2)(a_1^2a_3^2 - a_2^2) - (\lambda_1 - \chi\sigma\lambda_2)(a_1^2a_2^2 - a_3^2)},$$

$$a_1 = e^{-0.5\lambda_1 H}, \quad a_2 = e^{-0.5\lambda_2 H}, \quad a_3 = e^{-\lambda_2 H}.$$

$$\chi = \frac{\kappa_2}{\kappa_1}, \quad \lambda_{1,2} = \frac{2\pi}{H}\sqrt{1 + \frac{iU_0H}{2\pi\kappa_{1,2}}}. \tag{28}$$

In the simulations, κ_1 and κ_2 are set to be 1/60 and 1/6, respectively. The Peclet number Pe, defined as U_0H/κ_1 is fixed at 20. The present boundary scheme is applied to the conjugate interface. The temperature at such interface is considered to be unknown, which is to be determined by the constraint of the heat flux given by Eq. (26). The isotherm and the temperature profile in the conjugate channel are shown in Fig. 7. Good agreement can be observed between the present results and analytical solutions from Eq. (27). Five sets of $q = 0.01$, 0.25, 0.5, 0.75 and 0.99 are considered to test the accuracy of the scheme. The results shown in Fig. 8 again indicates a second-order spatial accuracy.

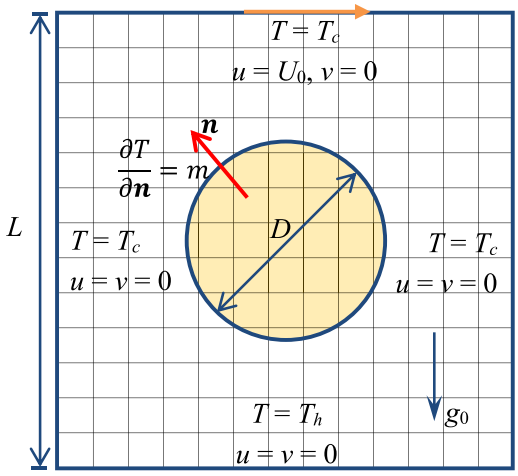

Fig. 20. Schematic of the mixed convection in a lid-driven cavity with an insulted cylinder.

3.3. Thermal diffusion between two concentrated cylinders

As shown in Fig. 9, the two cylinders have radii of R_o and R_i, respectively. The inner cylinder is specified with the constant temperature $T_i = 1.5$, and the outer one has a fixed heat flux at the interface, where the temperature gradient is $\partial T/\partial \boldsymbol{n} = m = 0.018$. Those settings are the same as Refs. [18,22]. The ratio of cylinder radii is defined as $\beta = R_i/R_o$, and we chose $\beta = 0.3$ and 0.5 in the simulation. The relaxation time of temperature distribution function is $\tau_T = 0.8$. At steady state, the temperature profile between the two cylinders can be obtained analytically as [18]

$$T(r) = T_i - mR_o \ln(r/R_i), \tag{29}$$

where r is the radial distance ranging from R_i to R_o.

The temperature profile between the two cylinders is shown in Fig. 10(a), where 40 lattices resolve R_o for the two cases. It can be found that the numerical results given by the present scheme agree well with the analytical solution. From Fig. 10(b), we can see the current scheme has second-order spatial accuracy for thermal convective flows with complex geometry, which preserves the precision of the original LBM. Furthermore, Fig. 11 delineates the relative error of temperature gradient. It can be observed that the convergence order of temperature gradient is between 1.0 and 2.0. From Eq. (21), the temperature gradient is a combination of the non-equilibrium distribution function, which is a low-order small quantity compared with the distribution function in LBM. And the temperature is a summation of the distribution functions according to the Eq. (10). Therefore, the second-order extrapolation of distribution functions by Eqs. (15) and (17) can guarantee a second-order accuracy of the temperature, but not always for a temperature gradient. In general, the temperature gradient would not affect the overall accuracy of the temperature fields, which is consistent with those by Zhang et al. [23].

3.4. Heat transfer in circular domains with a conjugate interface

The fluids are in the areas of $r < R_1$ and $R_1 < r < R_2$, with R_1 and R_2 denote the radii of the inner and outer cylinders, respectively (Fig. 12). At $r = R_2$, the temperature is specified as $T = \cos(4\theta)$ where θ is the polar angle. The interface at $r = R_1$ is conjugate described by the Eq. (26). The analytical solution for the temperature of this system can be written as [44]

$$T(r,\theta) = \begin{cases} b_1 r^4 \cos(4\theta), & 0 \le r \le R_1, \\ (b_2 r^4 + b_3 r^{-4})\cos(4\theta), & R_1 \le y \le R_2, \end{cases} \tag{30}$$

$$b_1 = \frac{2\sigma(\kappa_2/\kappa_1)R_1^{-8}R_2^{-4}}{(\sigma\kappa_2/\kappa_1+1)R_1^{-8} + (\sigma\kappa_2/\kappa_1-1)R_2^{-8}},$$
$$b_2 = \frac{(\sigma\kappa_2/\kappa_1+1)R_1^{-8}R_2^{-4}}{(\sigma\kappa_2/\kappa_1+1)R_1^{-8} + (\sigma\kappa_2/\kappa_1-1)R_2^{-8}},$$
$$b_3 = \frac{(\sigma\kappa_2/\kappa_1-1)R_2^{-4}}{(\sigma\kappa_2/\kappa_1+1)R_1^{-8} + (\sigma\kappa_2/\kappa_1-1)R_2^{-8}}. \tag{31}$$

In the simulations, σ is fixed as 1; κ_1 and κ_2 are set to be 1/60 and 1/6, respectively. Fig. 13 delineates the isotherm and the temperature profile of the conjugate system. It is observed that the present result agrees with those of the analytical solutions given by Eq. (30). The relative error of the temperature is depicted in Fig. 14. The convergence rate indicates that the present scheme is generally second-order accurate in space.

3.5. Natural convection in an annulus

As illustrated in Fig. 15, the outer cylinder maintains a uniform temperature $T_o = 0$, while the inner one has a heat flux at the surface with $\partial T/\partial \boldsymbol{n} = m = -1$. The flow system is subjected to a vertical gravity force field, and the fluid experiences a buoyancy force described by Eq. (4). In the simulation, the radii ratio $\beta = R_i/R_o$ is fixed at 0.5, where R_o and R_i are the radii of the inner and outer cylinders, respectively. The flow is governed by two non-dimensional parameters, i.e., the Rayleigh number Ra and Prandtl number Pr, which are defined as

$$Pr = \frac{\nu}{\kappa}, \qquad Ra = \frac{g_0 \alpha L^4 Q}{\kappa^2 \nu}, \tag{32}$$

where $L = (R_o - R_i)$ is the characteristic length resolved by 50 lattices, and $Q = -\kappa \partial T/\partial \boldsymbol{n}$ denotes the heat flux. The characteristic velocity of the flow can be expressed by

$$U_0 = \sqrt{\frac{g_0 \alpha L^2 Q}{\kappa}}. \tag{33}$$

In this test, we fix Pr, Ra and U_0 as 0.7, 5700 and 0.1, respectively.

Fig. 16 shows the isotherms and streamlines between the two cylinders. It can be observed that both flow and temperature fields are symmetric about the vertical centerline of concentric cylinders. A pair of crescent-shaped vortices are formed in the annulus, which is located at the shoulder of the inner cylinder. Furthermore, the fluid is heated by the inner surface, and a strong plume generates at the upper part of the annulus. All those indicates the flow is in convection dominated regime, which is consistent with previous studies [33–35]. We further show the temperature profile on the surface of the inner cylinder (see Fig. 17), and the results agree well with those reported in Refs. [33–35].

3.6. Flow around a heated cylinder with constant heat flux

As shown in Fig. 18, the circular cylinder with diameter D is located at (0.25 L, 0.5 H), where $L = 40$ D and $H = 20$ D are the length and width of the computational domain, respectively. The fluid with constant velocity U_0 and temperature T_c streams from left to right and is fully developed at the outlet. A temperature gradient with $\partial T/\partial \boldsymbol{n} = m = -1$ is specified at the cylinder surface. The flow is governed by the Reynolds number $Re = U_0 D/\nu$ and Prandtl number Pr. The Nusselt number Nu describing the heat transfer rate on the cylinder surface is defined as

$$Nu = \sqrt{\frac{-\frac{\partial T}{\partial \boldsymbol{n}} D}{(T - T_c)}}. \tag{34}$$

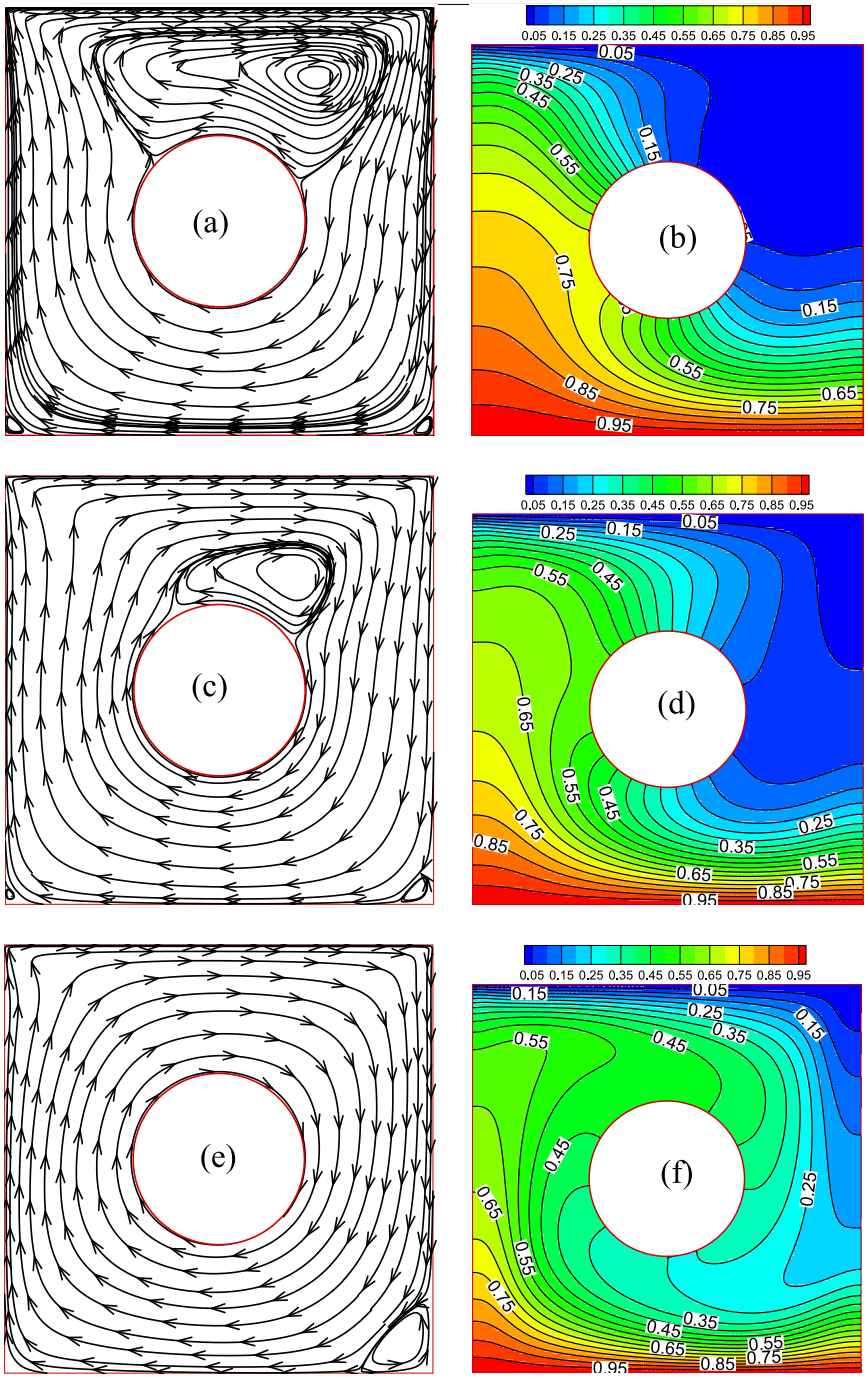

Fig. 21. Streamlines (left column) and isotherms (right column) in the lid-driven cavity with an insulted cylinder. The values of *Ri* are respectively 0.01 (a,b), 1 (c,d) and 10 (e,f).

In the simulation, we adopt $Re = 10$, 20, and 40; the Pr is fixed as 0.7; 50 lattices resolve the cylinder diameter.

Fig. 19 shows the isotherms around the cylinder and the distribution of Nusselt number along the cylinder surface. The isotherms (Fig. 19 (a,c,e)) are very dense in front of the cylinder, demonstrating a large temperature gradient and a high heat transfer rate in such region. As shown in Fig. 19 (b,d,f), the Nu always reaches the maximum and minimum values at the front and end rears of the cylinder, respectively. Moreover, the convection intensity is enhanced so that the region heated by the cylinder shrinks gradually for Re ranging from 10 to 40. Those observations are in good agreement with previous studies [33–35].

3.7. Thermal flow in a lid-driven cavity with a circular enclosure

As shown in Fig. 20, the circular enclosure with diameter $D = 0.4$ L is located at the center of the square cavity, where $L = 1$ is the side length of the cavity. The cold upper wall of $T = T_c$ constantly moves with the velocity of $U_0 = 0.05$. The hot bottom wall of $T = T_h$ is stationary. The two vertical walls are adiabatic and stationary. The average temperature of the flow is evaluated as $T_0 = (T_h + T_c)/2$. The immersed circular enclosure is adiabatic at the surface, i.e., $\partial T/\partial \boldsymbol{n} = m = 0$. In the simulation, the length of the cavity is resolved by 201 lattices, and the Pr is fixed as 0.7. The Re and Ra are defined as

$$Re = \frac{U_0 L}{\nu}, \qquad Ra = \frac{g_0 \alpha L^3 (T_h - T_c)}{\nu \kappa}, \tag{35}$$

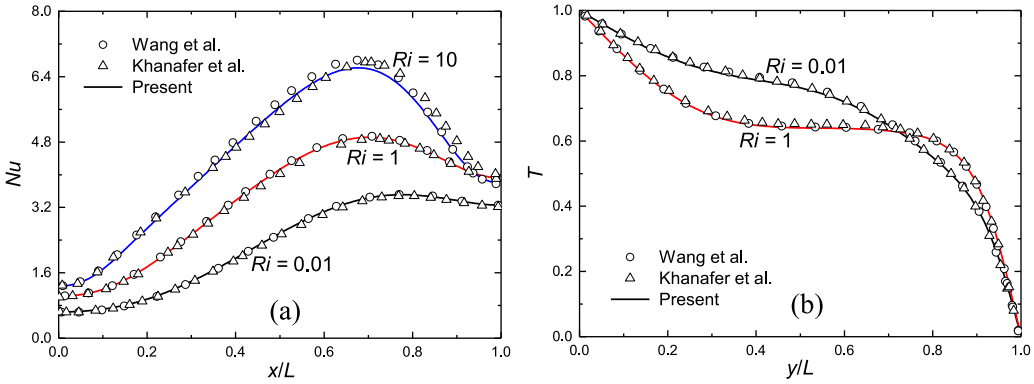

Fig. 22. The Nusselt number at the bottom wall of the cavity (a) and the temperature profile at $x/L = 0.15$ (b).

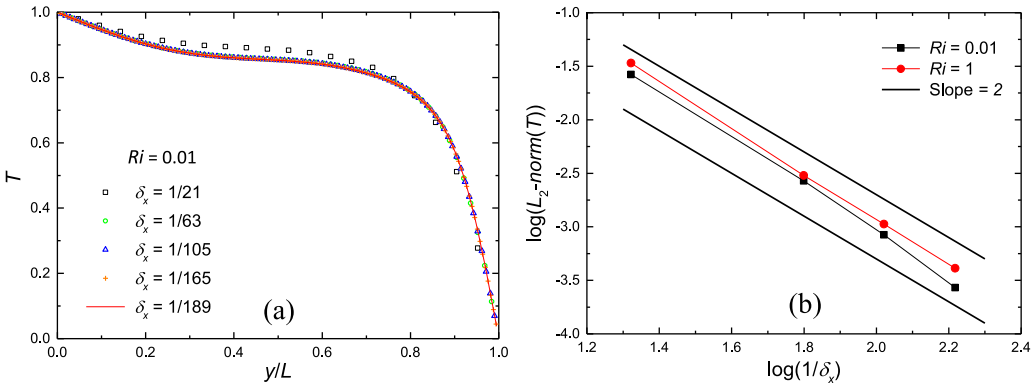

Fig. 23. The temperature profile at $x/L = 0.15$ with different grid resolutions (a) and the convergence rate of the temperature (b).

where Re is fixed as 100, and Ra = 70, 7000, and 70,000. The Richardson number is defined as $Ri = Ra/(Re^2Pr)$, the corresponding Ri values are 0.01, 1 and 10, respectively.

The streamlines and isotherms at different Ri are shown in Fig. 21. Duo to the moving upper cold wall, the flow and temperature profiles are all asymmetrical. At lower Richardson number ($Ri = 0.01$), a large vortex is generated between the cylinder and the upper wall. It shrinks and then removed with the increasing of Ri from 1 to 10. Meanwhile, the small vortex at the lower-left corner of the cavity disappears, and the lower-right corner grows with a certain degree. The cold region with a temperature lower than 0.1 is greatly suppressed at larger Ri. Particularly, the isotherms are generally perpendicular to the cylinder surface and the two vertical walls of the cavity, where adiabatic conditions are specified. Fig. 22 shows the Nusselt number at the bottom wall of the cavity and the temperature profile at $x/L = 0.15$. It can be observed that those results mentioned above are all in good agreement with those reported in Refs. [33,36].

We also evaluate the numerical accuracy of the present scheme in this case. Here, we take the temperature obtained with the finest grid as the reference solution since no analytical solution is available. Fig. 23(a) shows the temperature profile at $x/L = 0.15$ with five sets of grid resolutions. We can see the result can almost achieve mesh-independence at $\delta_x = 1/189$. The relative error of the temperature is then calculated by comparing with that of $\delta_x = 1/189$ according to Eq. (23). The convergence rate of the temperature is generally second-order, indicating again that the present scheme is second-order spatial accurate.

4. Conclusions

In this work, we proposed a curved lattice Boltzmann boundary scheme for thermal convective flows with Neuman boundary condition. The key idea is to obtain the intermediate distribution function at the intersection node for accomplishing the interpolation of the unknown temperature distribution function. In contrast to previous studies where the *temperature* is extrapolated from the fluid nodes, we extrapolated the *temperature distribution function* from the fluid nodes, and the extrapolation is lattice link-based. Furthermore, using the anti-bounce back rule, the distribution function at the intersection point can be all obtained. The Neumann boundary condition is then applied locally by the moments of the distribution functions. Those features contribute to the efficient implementation in the simulations. The second-order spatial accuracy of the present scheme is verified in the heat transfer in a channel flow and thermal diffusion between an annulus. Three additional thermal convective flow problems with Neumann boundary conditions, including the natural convection in an annulus, the thermal flow past a cylinder, and the mixed convection in a lid-driven cavity with a circular enclosure are further simulated to validate the present scheme for complex geometries. The simulation results are consistent with existing benchmark data obtained by other methods.

Declaration of Competing Interest

The authors declare that there is no conflict of interest.

CRediT authorship contribution statement

Shi Tao: Conceptualization, Methodology, Software, Writing - review & editing. **Ao Xu:** Data curation, Writing - original draft. **Qing He:** Visualization, Investigation. **Baiman Chen:** Writing - review & editing. **Frank G.F. Qin:** Supervision.

Acknowledgments

This work was supported by the National Natural Science Foundation of China (51906044 and 11902268), the Doctoral Start-up Foundation of Dongguan University of Technology, China (Grant No. GC300502-39), and the Foundation of National Key Laboratory under grant No. 614220119030103.

Supplementary materials

Supplementary material associated with this article can be found, in the online version, at doi:10.1016/j.ijheatmasstransfer.2020.119345.

References

[1] C.K. Aidun, J.R. Clausen, Lattice-Boltzmann method for complex flows, Annu. Rev. Fluid Mech. 42 (2010) 439–472.
[2] Q. Li, K.H. Luo, Q.J. Kang, Y.L. He, Q. Chen, Q. Liu, Lattice Boltzmann methods for multiphase flow and phase-change heat transfer, Prog. Energy Combust. Sci. 52 (2016) 62–105.
[3] A. Xu, L. Shi, T.S. Zhao, Accelerated lattice Boltzmann simulation using GPU and OpenACC with data management, Int. J. Heat Mass Transfer 109 (2017) 577–588.
[4] Y.L. He, Q. Liu, Q. Li, W.Q. Tao, Lattice Boltzmann methods for single-phase and solid-liquid phase-change heat transfer in porous media: a review, Int. J. Heat Mass Transfer 129 (2019) 160–197.
[5] A.E.F. Monfared, A. Sarrafi, S. Jafari, M. Schaffie, Linear and non-linear Robin boundary conditions for thermal lattice Boltzmann method: cases of convective and radiative heat transfer at interfaces, Int. J. Heat Mass Transfer 95 (2016) 927–935.
[6] A. Xu, L. Shi, H.D. Xi, Lattice Boltzmann simulations of three-dimensional thermal convective flows at high Rayleigh number, Int. J. Heat Mass Transfer 140 (2019) 359–370.
[7] A. Xu, L. Shi, H.D. Xi, Statistics of temperature and thermal energy dissipation rate in low-Prandtl number turbulent thermal convection, Phys. Fluids 31 (12) (2019) 125101.
[8] A.J. Ladd, Lattice-Boltzmann methods for suspensions of solid particles, Mol. Phys. 113 (17–18) (2015) 2531–2537.
[9] X. Yin, J. Zhang, An improved bounce-back scheme for complex boundary conditions in lattice Boltzmann method, J. Comput. Phys. 231 (11) (2012) 4295–4303.
[10] Z. Guo, C. Zheng, B. Shi, An extrapolation method for boundary conditions in lattice Boltzmann method, Phys. Fluids 14 (6) (2002) 2007–2010.
[11] H.B. Huang, X.Y. Lu, M.C. Sukop, Numerical study of lattice Boltzmann methods for a convection-diffusion equation coupled with Navier–Stokes equations, J. Phys. A Math. Theor. 44 (5) (2011) 055001.
[12] L. Wang, Y. Zhao, X. Yang, B. Shi, Z. Chai, A lattice Boltzmann analysis of the conjugate natural convection in a square enclosure with a circular cylinder, Appl. Math. Modell. 71 (2019) 31–44.
[13] E. Fattahi, M. Farhadi, K. Sedighi, Lattice Boltzmann simulation of natural convection heat transfer in eccentric annulus, Int. J. Therm. Sci. 49 (12) (2010) 2353–2362.
[14] R. Khazaeli, S. Mortazavi, M. Ashrafizaadeh, Application of a ghost fluid approach for a thermal lattice Boltzmann method, J. Comput. Phys. 250 (2013) 126–140.
[15] M. Mozafari-Shamsi, M. Sefid, G. Imani, Application of the ghost fluid lattice Boltzmann method to moving curved boundaries with constant temperature or heat flux conditions, Comput. Fluids 167 (2018) 51–65.
[16] A. Tiwari, S.P. Vanka, A ghost fluid Lattice Boltzmann method for complex geometries, Int. J. Numer. Methods Fluids 69 (2) (2012) 481–498.
[17] T. Zhang, B. Shi, Z. Guo, Z. Chai, J. Lu, General bounce-back scheme for concentration boundary condition in the lattice-Boltzmann method, Phys. Rev. E 85 (1) (2012) 016701.
[18] Q. Chen, X. Zhang, J. Zhang, Improved treatments for general boundary conditions in the lattice Boltzmann method for convection-diffusion and heat transfer processes, Phys. Rev. E 88 (3) (2013) 033304.
[19] C.H. Liu, K.H. Lin, H.C. Mai, C.A. Lin, Thermal boundary conditions for thermal lattice Boltzmann simulations, Comput. Math. Appl. 59 (7) (2010) 2178–2193.
[20] J. Huang, W.A. Yong, Boundary conditions of the lattice Boltzmann method for convection–diffusion equations, J. Comput. Phys. 300 (2015) 70–91.
[21] J. Huang, Z. Hu, W.A. Yong, Second-order curved boundary treatments of the lattice Boltzmann method for convection–diffusion equations, J. Comput. Phys. 310 (2016) 26–44.
[22] X. Meng, Z. Guo, Boundary scheme for linear heterogeneous surface reactions in the lattice Boltzmann method, Phys. Rev. E 94 (5) (2016) 053307.
[23] L. Zhang, S. Yang, Z. Zeng, J.W. Chew, Consistent second-order boundary implementations for convection-diffusion lattice Boltzmann method, Phys. Rev. E 97 (2) (2018) 023302.
[24] L. Li, R. Mei, J.F. Klausner, Lattice Boltzmann models for the convection-diffusion equation: D2Q5 vs D2Q9, Int. J. Heat Mass Transfer 108 (2017) 41–62.
[25] L. Li, R. Mei, J.F. Klausner, Boundary conditions for thermal lattice Boltzmann equation method, J. Comput. Phys. 237 (2013) 366–395.
[26] H. Lamarti, M. Mahdaoui, R. Bennacer, A. Chahboun, Numerical simulation of mixed convection heat transfer of fluid in a cavity driven by an oscillating lid using lattice Boltzmann method, Int. J. Heat Mass Transfer 137 (2019) 615–629.
[27] A. D'Orazio, A. Karimipour, A useful case study to develop lattice Boltzmann method performance: Gravity effects on slip velocity and temperature profiles of an air flow inside a microchannel under a constant heat flux boundary condition, Int. J. Heat Mass Transfer 136 (2019) 1017–1029.
[28] P. Lallemand, L.S. Luo, Theory of the lattice Boltzmann method: Dispersion, dissipation, isotropy, Galilean invariance, and stability, Phys. Rev. E 61 (6) (2000) 6546.
[29] Z. Guo, C. Zheng, B. Shi, Discrete lattice effects on the forcing term in the lattice Boltzmann method, Phys. Rev. E 65 (4) (2002) 046308.
[30] K. Suzuki, T. Kawasaki, N. Furumachi, Y. Tai, M. Yoshino, A thermal immersed boundary–lattice Boltzmann method for moving-boundary flows with Dirichlet and Neumann conditions, Int. J. Heat Mass Transfer 121 (2018) 1099–1117.
[31] F. Dubois, P. Lallemand, M.M. Tekitek, On anti bounce back boundary condition for lattice Boltzmann schemes, Comput. Math. Appl. (2019).
[32] S. Tao, Q. He, B. Chen, X. Yang, S. Huang, One-point second-order curved boundary condition for lattice Boltzmann simulation of suspended particles, Comput. Math. Appl. 76 (7) (2018) 1593–1607.
[33] Y. Wang, C. Shu, L.M. Yang, Boundary condition-enforced immersed boundary-lattice Boltzmann flux solver for thermal flows with Neumann boundary conditions, J. Comput. Phys. 306 (2016) 237–252.
[34] T. Guo, E. Shen, Z. Lu, Y. Wang, L. Dong, Implicit heat flux correction-based immersed boundary-finite volume method for thermal flows with Neumann boundary conditions, J. Comput. Phys. 386 (2019) 64–83.
[35] W. Ren, C. Shu, W. Yang, An efficient immersed boundary method for thermal flow problems with heat flux boundary conditions, Int. J. Heat Mass Transfer 64 (2013) 694–705.
[36] K. Khanafer, S.M. Aithal, Laminar mixed convection flow and heat transfer characteristics in a lid driven cavity with a circular cylinder, Int. J. Heat Mass Transfer 66 (2013) 200–209.
[37] Y.H. Qian, D. d'Humières, P. Lallemand, Lattice BGK models for Navier-Stokes equation, Europhys. Lett. 17 (6) (1992) 479.
[38] Y. Zhao, B. Shi, Z. Chai, L. Wang, Lattice Boltzmann simulation of melting in a cubical cavity with a local heat-flux source, Int. J. Heat Mass Transfer 127 (2018) 497–506.
[39] Y. Hu, D. Li, S. Shu, X. Niu, Study of multiple steady solutions for the 2D natural convection in a concentric horizontal annulus with a constant heat flux wall using immersed boundary-lattice Boltzmann method, Int. J. Heat Mass Transfer 81 (2015) 591–601.
[40] S. Tao, B. Chen, H. Xiao, S. Huang, Lattice Boltzmann simulation of thermal flows with complex geometry using a single-node curved boundary condition, Int. J. Therm. Sci. 146 (2019) 106112.
[41] G. Le, O. Oulaid, J. Zhang, Counter-extrapolation method for conjugate interfaces in computational heat and mass transfer, Phys. Rev. E 91 (3) (2015) 033306.
[42] Z. Wang, F. Colin, G. Le, J. Zhang, Counter-extrapolation method for conjugate heat and mass transfer with interfacial discontinuity, Int. J. Numer. Methods Heat Fluid Flow 27 (10) (2017) 2231–2258.
[43] S. Cui, N. Hong, B. Shi, Z. Chai, Discrete effect on the halfway bounce-back boundary condition of multiple-relaxation-time lattice Boltzmann model for convection-diffusion equations, Phys. Rev. E 93 (4) (2016) 043311.
[44] L. Li, C. Chen, R. Mei, J.F. Klausner, Conjugate heat and mass transfer in the lattice Boltzmann equation method, Phys. Rev. E 89 (4) (2014) 043308.
[45] Z. Chai, T.S. Zhao, Nonequilibrium scheme for computing the flux of the convection-diffusion equation in the framework of the lattice Boltzmann method, Phys. Rev. E 90 (1) (2014) 013305.